Catalysis Science & Technology

PAPER

View Article Online
View Journal | View Issue

Cite this: *Catal. Sci. Technol.*, 2014, **4**, 4396

Magnetically separable reduced graphene oxide/iron oxide nanocomposite materials for environmental remediation

Teo Peik-See,[a] Alagarsamy Pandikumar,*[a] Lim Hong Ngee,[bc] Huang Nay Ming*[a] and Chia Chin Hua[d]

Magnetically separable reduced graphene oxide/iron oxide (rGO/Fe_3O_4) nanocomposite materials were synthesized at room temperature through a facile, eco-friendly and cost-effective approach. The prepared nanocomposite materials were characterized by different techniques. X-ray diffraction analysis revealed the formation of the rGO/Fe_3O_4 nanocomposites, while transmission electron microscope images showed that the Fe_3O_4 nanoparticles with an average size of 10 nm were embedded uniformly on the surface of rGO sheets. The synthesized rGO/Fe_3O_4 nanocomposite materials were found to be super-paramagnetic in nature at room temperature. The photocatalytic performance of the rGO/Fe_3O_4 nanocomposite materials was investigated under natural sunlight irradiation using methylene blue (MB) as a model target organic pollutant. The rGO/Fe_3O_4 showed better adsorption behaviour and excellent photocatalytic activity towards the degradation of MB, when compared to other samples such as rGO and pristine Fe_3O_4 nanoparticles. This enhanced photocatalytic activity could be attributed to the synergistic effect that arises between the rGO and Fe_3O_4, which significantly reduces charge recombination. Moreover, the rGO/Fe_3O_4 nanocomposite materials exhibited good sustainability, which was evidenced by their consistent photocatalytic performance and the absence of any observable changes in morphology, even after eight cycles of operation during photocatalytic experiments. The overall results of the study indicate that these newly prepared photocatalytically stable and magnetically separable rGO/Fe_3O_4 nanocomposites could be potentially utilized for many environmental remediation applications.

Received 22nd June 2014,
Accepted 2nd August 2014

DOI: 10.1039/c4cy00806e

www.rsc.org/catalysis

1. Introduction

The requirement for fresh water is paramount for all living organisms, including human beings, and its availability is a major problem throughout the world at present. In the future, this issue will become even more pressing, owing to rapid industrialization and population growth. In particular, the rapid growth of the textile and dying industries has caused critical environmental problems, as some of the dye effluents from these industries can pollute ground water resources, and their utilisation has many toxic and harmful effects on human beings. In this respect, different types of photocatalytic materials *viz.* free-standing photocatalysts, doped photocatalysts, dual semiconductors and noble metal deposited photocatalysts have been developed, for the treatment and purification of dye-contaminated waste water. Among them, very few have been reported that use a physical separation technique, by which the photocatalysts can be separated easily from the reaction medium. The major disadvantage of a colloidal photocatalytic system is the complicated separation of the catalyst from the reaction medium. To overcome this issue, magnetic separation of the photocatalyst has been proposed as a promising solution. Magnetically separable photocatalytic systems are more advantageous than colloidal photocatalytic systems, as they do not require filtration or centrifugation for the removal of the catalyst from the reaction medium. Hence, the physical separation of a photocatalyst can easily be achieved using these magnetically separable photocatalysts.

Graphene, a single layer of sp^2-bonded carbon atoms arranged in a two-dimensional (2D) honeycomb structure, possesses a high surface area and excellent thermal, mechanical and electrical properties; these make it a good supporting

[a] *Department of Physics, Faculty of Science, University of Malaya, 50603 Kuala Lumpur, Malaysia. E-mail: pandikumarinbox@gmail.com, huangnayming@um.edu.my; Tel: +6 0163301609*
[b] *Department of Chemistry, Faculty of Science, Universiti Putra Malaysia, 43400 UPM Serdang, Selangor, Malaysia*
[c] *Functional Device Laboratory, Institute of Advanced Technology, Universiti Putra Malaysia, 43400 UPM Serdang, Selangor, Malaysia*
[d] *School of Applied Physics, Faculty of Science and Technology, Universiti Kebangsaan Malaysia, 43600 Bangi, Selangor, Malaysia*

material for inorganic nanoparticles used in various energy and environmental applications.[1,2] The combination of graphene with the inorganic nanoparticles liberates new functional hybrid materials, which possess complementary behaviours to each constituent and thus open up new opportunities for the enhancement of wider applications.[3,4] These graphene-based nanocomposite materials not only show significant improvements in electrochemical activity, but also exhibit high photocatalytic activity, because the unique surface properties of graphene enable it to accept electrons to impede the recombination of photoinduced electrons and holes; additionally, it allows the absorption of dye through π–π conjugation between the dyes and aromatic regions of the graphene, which can be of use in environmental remediation applications.[5–7] Although these graphene-based nanocomposites (*e.g.* rGO–TiO_2, rGO–ZnO, *etc.*) display excellent performances in photocatalytic systems, the problems associated with the recovery, reuse and separation of the catalysts from the reaction medium still exist after the photodegradation process, because the good dispersive properties of these materials means that they are inconvenient to recycle. Hence, the introduction of magnetic nanophotocatalytic materials into the graphene sheets can provide convenient magnetic separation, in order to remove and recycle the magnetic nanocomposite catalysts under an external magnetic field.[8,9] Recently, magnetite (Fe_3O_4) nanoparticles have attracted much attention because of their low-cost, eco-friendly and simple preparation, and because they show desirable properties of strong super-paramagnetic and electrical conductivities, as well as optical and chemical properties.[10,11] Hence, they find potential applications in the areas of biosensors,[12] catalysis,[13,14] supercapacitors[15] and photocatalysis.[16] A few studies have shown that bare Fe_3O_4 nanoparticles are photocatalytically inactive under solar irradiation, owing to the rapid aggregation caused by their high surface area and magnetic interactions between the particles; this leads to the formation of larger Fe_3O_4 particles and hence impairs their chemical and photocatalytic properties. The incorporation of these Fe_3O_4 nanoparticles into graphene sheets is a promising way to overcome this limitation, as it prevents the serious agglomeration of magnetite nanoparticles,[17,18] leading to a high photocatalytic performance under sunlight due to the contribution of improved photo-induced charge separation efficiency within the Fe_3O_4 nanoparticles.[19]

In this investigation, we report a green, facile and cost-effective method to prepare, at room temperature, rGO/Fe_3O_4 nanocomposite materials which are magnetically separable and recyclable. The photocatalytic performances of the prepared rGO/Fe_3O_4 nanocomposite materials were evaluated in the degradation of a model organic dye, methylene blue (MB). The influence of different contents of Fe_3O_4 nanoparticles in the magnetically separable (rGO/Fe_3O_4) photocatalysts was studied, to optimize the Fe_3O_4 nanoparticles for maximum photodegradation efficiency. The magnetically separable rGO/Fe_3O_4 photocatalysts showed better photocatalytic performances when compared to control samples such as rGO and pristine Fe_3O_4 nanoparticles. Moreover, the separated rGO/Fe_3O_4 nanoparticles were reused for several photodegradation experiment cycles, indicating their sustainability.

2. Experimental methods

2.1 Materials

Chemical reagents such as sulphuric acid (H_2SO_4, 98%), potassium permanganate ($KMnO_4$, 99.9%), hydrogen peroxide (H_2O_2, 30%), iron(II) sulphate ($FeSO_4{\cdot}7H_2O$, 99.5%), methylene blue (MB) and ammonium hydroxide (NH_4OH, 25%) were purchased from Systerm and used as received. Graphite flakes were purchased from Ashbury Inc. All other chemicals used in this work were of analytical grade. Unless otherwise specified, deionized double distilled water was used for all the experiments.

2.2 Preparation of graphene oxide

Graphene oxide (GO) was synthesized from graphite by adopting the simplified Hummer's method.[20] Briefly, 3 g of graphite flakes were oxidatively treated with 400 mL of H_2SO_4 and 18 g of $KMnO_4$ for 5 min under magnetic stirring, leading to the development of graphite oxide. However, to ensure complete oxidation of the graphite, the solution was stirred for another 3 days. During the oxidation process, a colour change of the solution from dark purplish-green to dark brown was observed. Then, H_2O_2 solution was added to stop the oxidation process, during which the colour of the solution changed to bright yellow; this indicated the highly oxidized level of the graphite. The obtained graphite oxide was washed 3 times with an aqueous solution containing 1 M of HCl, and this procedure was repeated until the solution pH reached 4–5. At this pH, the graphite oxide experienced exfoliation, which resulted in a thickening of the GO solution and formation of a GO gel. Finally, the GO gel was freeze-dried to obtain solid GO.

2.3 Preparation of rGO/Fe_3O_4

rGO/Fe_3O_4 nanocomposites with different weight ratios of rGO and Fe_3O_4 were prepared by a simple *in situ* chemical synthesis method. Typically, 25 mg of GO was dispersed in deionized double distilled (DD) water under stirring, and this was then subjected to sonication for 20 min. Then, 25% of NH_4OH solution was added drop-wise into the GO solution until the pH reached ~11–12. Following this, a specific quantity of $FeSO_4$ solution was slowly added to the above solution containing GO under magnetic stirring, and the solution was left overnight at room temperature. The obtained black solution containing rGO/Fe_3O_4 nanocomposites was centrifuged and washed with DD water for 10 min at 4000 rpm, and this procedure was repeated three times, to remove excess NH_4OH present in the solution. Finally the solution was dried in a vacuum oven. The same protocol was followed to prepare Fe_3O_4 nanoparticles, in the absence of GO. Meanwhile the

rGO was prepared using the same procedure, without adding $FeSO_4$ solution. The weight ratios of the GO and $FeSO_4$ are given in Table 1.

2.4 Characterization techniques

The size, shape and morphology of the rGO/Fe_3O_4 nanocomposites were analyzed with a high resolution transmission electron microscope (HR-TEM). Raman and photoluminescence spectral data were collected using a Renishaw 2000 inVia Raman microscope system, with an argon ion laser emitting at 514.5 nm. A Siemens-D5000 X-ray diffractometer with copper Kα radiation (λ = 1.5418 Å) at a scan rate of 0.02 degree s^{-1} was used for X-ray diffraction (XRD) analysis. A Thermo Scientific Evolution-300 UV-vis absorption spectrophotometer was employed for absorption studies, in a spectral range of 190–900 nm. Magnetization measurements were carried out at room temperature using a Lakeshore-736 vibrating sample magnetometer (VSM), with a maximum magnetic field of 10 kOe.

2.5 Photocatalytic studies

The photocatalytic performances of the prepared rGO/Fe_3O_4 samples were evaluated with methylene blue (MB) dye as a model target organic pollutant, under natural sunlight irradiation. The photocatalytic experiments were performed on bright sunny days from 9 a.m. to 2 p.m. All the prepared photocatalyst materials (2 mg) were separately dispersed in 12 mL of MB solution (10 mg L^{-1}) under stirring and left overnight (12 h) at room temperature, in order to study their adsorption behaviours. Prior to the sunlight irradiation, the MB solution was stirred for 1 h in the dark, thereby allowing the system to attain an adsorption–desorption equilibrium between the photocatalyst and the MB molecules. At given time intervals of irradiation, 2 mL of irradiated MB dye solution was periodically withdrawn, and at the end of the experiment the photocatalyst was removed from the reaction solution by magnetic separation using a permanent magnet. The equilibrium concentration of MB dye in the reaction solution for each sample was determined with a UV-visible absorption spectrophotometer, by measuring the absorbance intensity at 662 nm during the photocatalytic degradation process. To study the sustainability of the photocatalysts, the rGO/Fe_3O_4 was collected by applying a magnetic field and washed with DI water, before being re-dispersed into fresh MB solution for the next cycle.

Table 1 Weight ratios of GO and $FeSO_4$ used for the preparation of rGO/Fe_3O_4

Sample	m_{GO} (mg)	m_{FeSO4} (mg)	Weight ratio (GO : $FeSO_4$)
G1F2	25	50	1 : 2
G1F5	25	125	1 : 5
G1F10	25	250	1 : 10
G1F20	25	500	1 : 20
G1	25	—	—
F20	—	500	—

The photodegradation rates and MB dye removal efficiencies under natural sunlight irradiation of different photocatalysts were calculated using the following equations.

$$\text{Photodegradation efficiency } (\%) = \frac{C}{C_0} \times 100 \quad (1)$$

$$\text{Dye removal efficiency } (\%) = \left(1 - \frac{C_t}{C_0}\right) \times 100 \quad (2)$$

where C_0 represents the initial concentration of MB, and C_t is the concentration of MB at reaction time 't'.

3. Results and discussion

3.1. Morphological characterization of rGO/Fe_3O_4 nanocomposites

The TEM images of Fe_3O_4 and rGO/Fe_3O_4 nanocomposite materials before and after the 8 cycles of photocatalytic experiments are shown in Fig. 1 and 2(a–e), respectively. The TEM images clearly indicate that the Fe_3O_4 nanoparticles are uniformly embedded on the surface of the rGO sheets in all the nanocomposite materials, and that no significant changes in the morphology of the rGO/Fe_3O_4 nanocomposite are observed before and after the photocatalytic studies (Fig. 1 and 2). The decreasing tendency of the Fe_3O_4 to agglomerate, and the restacking of the rGO sheets, are vital in determining the photocatalytic activity of the rGO/Fe_3O_4 nanocomposite. The lattice-resolved TEM image of the rGO/Fe_3O_4 nanocomposite reveals the presence of clear atomic lattice-fringes of Fe_3O_4 nanoparticles on the surface of the rGO sheets (Fig. 2f). The estimated lattice-fringe or fringe values of the magnetic Fe_3O_4 nanoparticles are 2.533 Å and 1.643 Å, which can be respectively indexed to the (311) plane (2.530 Å) and (511) plane (1.614 Å); this is compatible with the XRD observations. The increase in concentration of the $FeSO_4$ nanoparticles during the preparation of the nanocomposite led to an increase in the particle sizes of Fe_3O_4, in the order of G1F2 < G1F5 < G1F10 < G1F20 (Fig. 1(b–f)). This indicates that the aggregation tendency of the Fe_3O_4 nanoparticles in the rGO/Fe_3O_4 nanocomposite becomes greater with an increasing $FeSO_4$ precursor concentration. Among the different nanocomposite materials, G1F20 showed the most aggregation of Fe_3O_4 nanoparticles (Fig. 1(f)), while G1F2 exhibited a good distribution of Fe_3O_4 nanoparticles on the surface of the rGO sheets (Fig. 1(c)).

3.2. XRD studies of Fe_3O_4/rGO nanocomposites

Fig. 3 portrays the representative XRD patterns of the G1, F20 and rGO/Fe_3O_4 nanocomposites, which coincide with the results from the HRTEM image (Fig. 2(f)), and confirm the formation of Fe_3O_4 crystallites in the nanocomposites. The XRD pattern of F20 (Fig. 3(e)) displays a series of diffraction peaks at 2θ = 30.2°, 35.6°, 43.3°, 53.7°, 57.3°, and 62.8°, corresponding to the reflections from the (220), (311), (400),

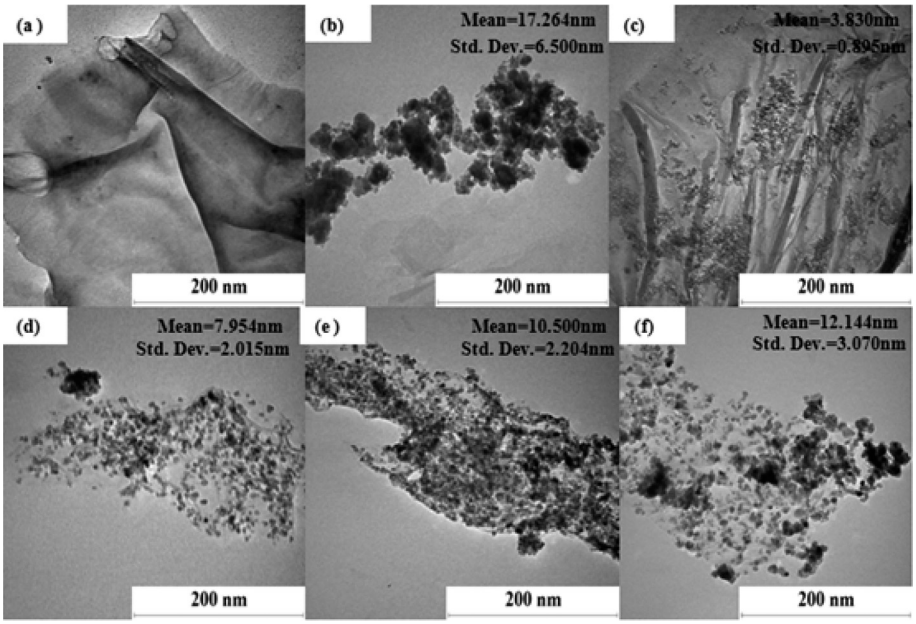

Fig. 1 TEM images of G1 (a), F20 (b), G1F2 (c), G1F5 (d), G1F10 (e) and G1F20 (f) before the photocatalytic process.

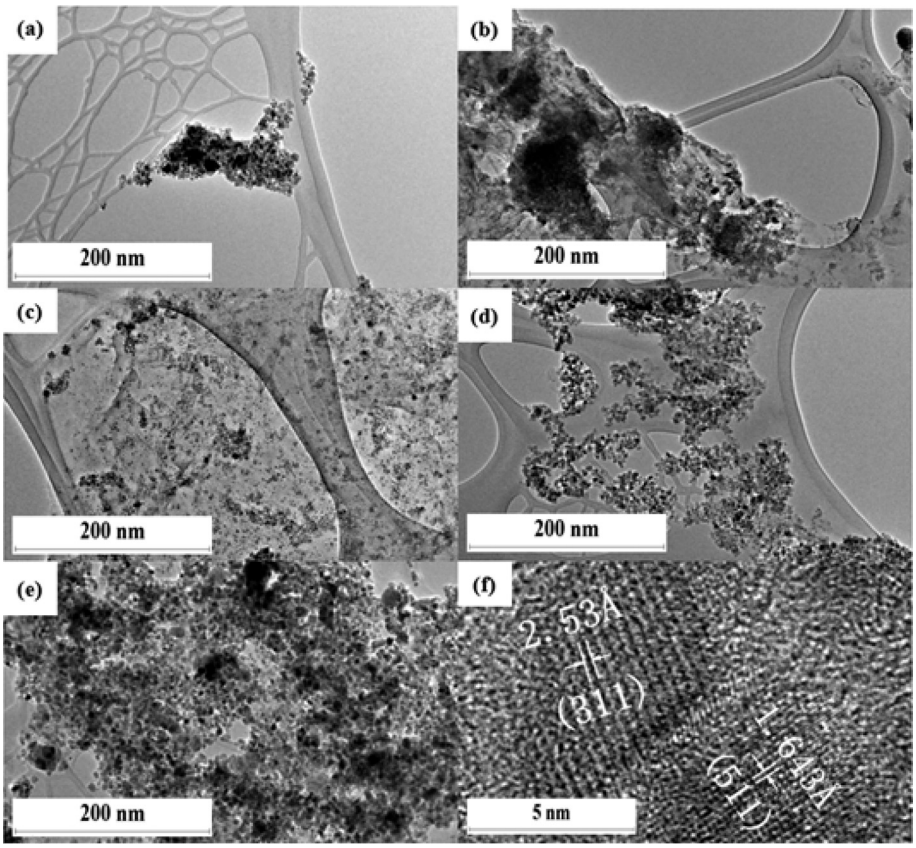

Fig. 2 HR-TEM images of F20 (a), G1F2 (b), G1F5 (c), G1F10 (d) and G1F20 Fe_3O_4/rGO (e) after 8 cycles of the photocatalytic process, and G1F20 (f) at a higher magnification.

(422), (511), and (440) crystal planes of the cubic spinel structure of magnetite Fe_3O_4. A sharp peak observed in G1 (Fig. 3(a)) at $2\theta = 10.8°$ is assigned to the (001) reflection of GO, which indicates that the GO was incompletely reduced to rGO. For the sample rGO/Fe_3O_4 containing Fe^{2+} ions, this (001) plane was absent, which suggests that Fe^{2+} plays an

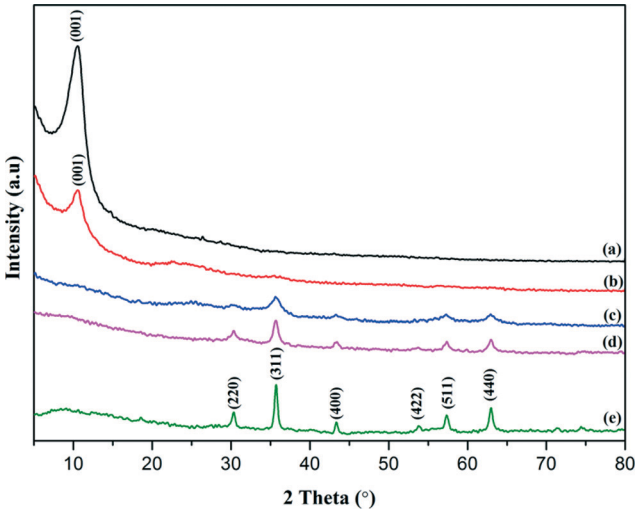

Fig. 3 XRD patterns of G1 (a), G1F2 (b), G1F5 (c), G1F10 (d), and (e) F20.

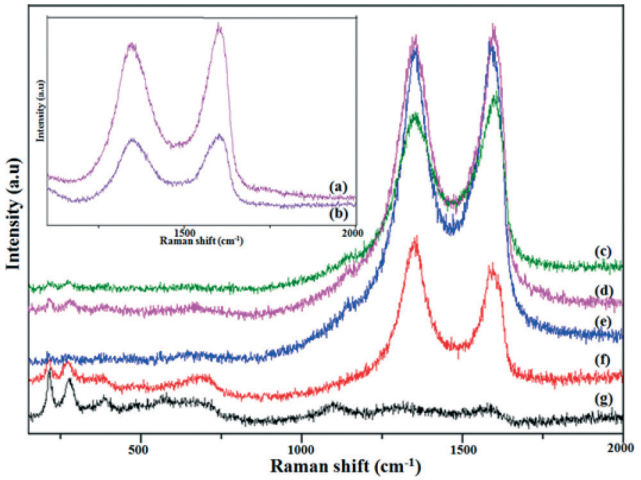

Fig. 4 Raman spectra for GO (a), G1 (b), G1F2 (c), G1F5 (d), G1F10 (e), G1F20 (f) and F20 (g).

important role as a reducing agent in the redox reaction of nanocomposite fabrication (Fig. 3(b)). For sample G1F2, this sharp XRD line was observed while the diffraction peaks for Fe_3O_4 were not detected, owing to the low amount of Fe^{2+} ions in the nanocomposite resulting from the partial reduction of GO. However, when increasing the content of Fe_3O_4, the five typical characteristic diffraction peaks of Fe_3O_4 and the disappearance of the graphitic peak were clearly observed for G1F5 and G1F10 (Fig. 3(c–d)). This can be ascribed to the formation of van der Waals and π–π stacking interactions between the rGO sheets being prevented by the Fe_3O_4 nanoparticles.[21]

3.3. Raman spectral studies of Fe_3O_4/rGO nanocomposites

Raman spectroscopy is an excellent tool to investigate the ordered and disordered crystal structures of carbonaceous materials, *viz.* graphene, graphene oxide and reduced graphene oxide. Raman spectra of the GO, G1 and rGO/Fe_3O_4 photocatalyst materials were recorded, and are presented in Fig. 4. Fig. 4 (inset) shows the existence of a D band at around 1350 cm^{-1}, which can be ascribed to the sp^3 defects, while the G band at around 1580 cm^{-1} is related to the in-plane vibration of sp^2 carbon atoms in a 2D hexagonal lattice of GO and rGO. The observed positions and intensities of the D and G bands highly influence the structural transformation in carbonaceous materials. The I_D/I_G ratio of the rGO/Fe_3O_4 nanocomposites (0.92–1.15) showed remarkable increases (Fig. 4(c–f)) over that of GO (0.91); this is due to the higher amount of Fe_3O_4 in the nanocomposite. The relatively high intensity of the D band when compared to the G band of rGO/Fe_3O_4 indicates the presence of localized sp^3 defects within sp^2 clusters during the functionalization process of the exfoliated GO.[22,23] Additionally, the characteristic Raman peak around 670 cm^{-1} suggests the presence of magnetite (Fe_3O_4) (Fig. 4(c–g)). It is known from an earlier report that the observed broad peak at ~670 cm^{-1} is due to the presence of magnetite nanoparticles in the rGO/Fe_3O_4 nanocomposites.[24]

3.4. Magnetic behaviour of Fe_3O_4/rGO nanocomposites

Studying the magnetic behaviour of the prepared magnetically separable rGO/Fe_3O_4 nanocomposites is essential. In this respect, VSM analysis was carried out at room temperature for both the bare Fe_3O_4 nanoparticles and the rGO/Fe_3O_4 nanocomposites, and the results are shown in Fig. 5. The bare Fe_3O_4 nanoparticles and the rGO/Fe_3O_4 nanocomposites showed typical S-like curve magnetization hysteresis loops with no coercivity, inferring that they exhibit super-paramagnetism, while their magnetization behaviours were removed in the absence of the applied magnetic field. The saturation magnetization (Ms) of the rGO/Fe_3O_4 nanocomposites increased from 1.63 emu g^{-1} to 30.30 emu g^{-1} with a increase in the

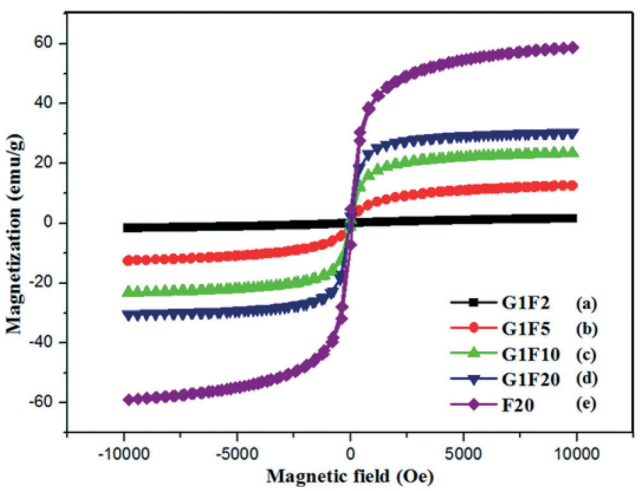

Fig. 5 VSM magnetization curves of G1F2 (a), G1F5 (b), G1F10 (c), G1F20 (d) and F20 (e).

content of Fe_3O_4 nanoparticles in the rGO sheets. The saturated magnetization value observed for the pristine Fe_3O_4 nanoparticles was 58.70 emu g^{-1}, which was higher than that of the magnetic rGO/Fe_3O_4 nanocomposites. This can be attributed to the presence of graphene in the nanocomposites.[25]

3.5. Photoluminescence studies of rGO/Fe_3O_4 nanocomposites

Photoluminescence (PL) was used to study the electronic and optical properties of the nanocomposites, including the migration, transfer and recombination of electron–hole pair of the photoinduced semiconductor. Fig. 6 shows the room temperature PL spectra of rGO, the rGO/Fe_3O_4 nanocomposites and Fe_3O_4. It was observed from the PL spectra that the rGO and rGO/Fe_3O_4 nanocomposites exhibited lower PL intensities than that of the bare Fe_3O_4 nanoparticles. Fe_3O_4 is an indirect band gap semiconductor with a narrow optical gap value of 1.4 eV.[26] This narrowness value arises from the d orbitals, suggesting that Fe_3O_4 exhibits a high electrical conductivity with an almost metallic nature at room temperature, but that the low charge carrier (electron and hole) mobility in Fe_3O_4 may lead to an increase in electron–hole recombination. Therefore, the higher PL intensity of the bare Fe_3O_4 is due to the recombination of excited electrons and holes, whereas the lower PL emission intensities of rGO and the Fe_3O_4/rGO nanocomposites are due to the lower charge recombination rates. This suggests that graphene has a tendency to greatly influence the PL intensities of rGO/Fe_3O_4 nanocomposites, owing to its 2D hexagonal π-conjugation structure and excellent electronic conductivity. The high charge mobility of graphene means that it acts as an electron acceptor for the photo-excited electrons from Fe_3O_4, leading to a low charge recombination rate.[27–29] Among the prepared nanocomposites and rGO, G1F2 has the lowest PL intensity, which indicates that G1F2 efficiently suppresses electron–hole pair recombination and promotes charge separation; these are highly beneficial for photocatalytic applications. The synergistic effect[30] between graphene and Fe_3O_4 nanoparticles in the G1F2 nanocomposite allows graphene to capture or trap the photo-induced electrons from the conduction band of the Fe_3O_4 through the extended π-conjugation carbon network, and consequently restrict the flash recombination of electron–hole pair. Therefore, G1F2 is expected to show higher photocatalytic activity when compared to the other nanocomposites.[31] However, further increasing the Fe_3O_4 content in the rGO/Fe_3O_4 nanocomposite results in a higher PL intensity. The Fe_3O_4 nanoparticles possess large surface energies, and hence they tend to aggregate to minimize these surface energies. Thus, an excess amount of Fe_3O_4 nanoparticles in the rGO/Fe_3O_4 nanocomposite may lead to aggregation of the nanoparticles, resulting in larger particles.[32] Consequently, increasing the amount of Fe_3O_4 nanoparticles in the rGO/Fe_3O_4 nanocomposite introduces new charge recombination centres for photoinduced charge separation, and as a consequence this decreases the photocatalytic efficiency.

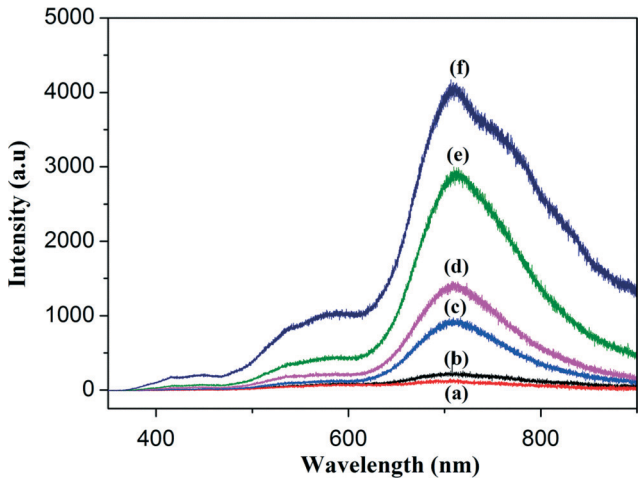

Fig. 6 Room temperature photoluminescence (PL) spectra of G1F2 (a), rGO (b), G1F5 (c), G1F10 (d), G1F20 (e) and F20 (f).

3.6. Photocatalytic activity of magnetically separable rGO/Fe_3O_4 nanocomposites for the degradation of methylene blue

The photocatalytic performances of the prepared photocatalytic materials *viz.* rGO, Fe_3O_4 and magnetically separable rGO/Fe_3O_4 nanocomposites were separately evaluated for the degradation of a model dye pollutant, methylene blue (MB) under natural sunlight irradiation for 5 h. The results of the photodegradation study are shown in Fig. 7(a). During the photocatalytic experiments, the bare Fe_3O_4 nanoparticles achieved only 57% photodegradation even after 5 h of sunlight irradiation (Fig. 7(a)). The poor photocatalytic performance of the bare Fe_3O_4 nanoparticles can be ascribed to the aggregation caused by the high surface area of Fe_3O_4 nanoparticles and the magnetic interactions between the particles, which lead to the formation of larger sized particles.[33] Interestingly, a maximum photodegradation of MB was observed at 1 h light irradiation when a photocatalyst of Fe_3O_4 nanoparticles, incorporated into reduced graphene oxide sheets, was used. To optimize the Fe_3O_4 content for maximum photodegradation of MB dye, photocatalytic experiments were carried out with different compositions of rGO and Fe_3O_4. Among the photocatalysts, G1F2 exhibited excellent photocatalytic activity; almost 89% of the MB was decolourized after 30 min and 100% after 1 h light irradiation. GIF5, GIF10 and GIF 20 achieved 100% degradation of MB after 2 h of irradiation. Meanwhile, the bare Fe_3O_4 nanoparticle photocatalyst could achieve only 57% MB dye removal efficiency. The maximum photocatalytic activity exhibited by the rGO/Fe_3O_4 nanocomposite photocatalysts is due to the emergence of synergistic effects in the rGO/Fe_3O_4 during the photocatalytic reaction *i.e.* efficient photogenerated charge transfer from Fe_3O_4 to the graphene sheets, which facilitates increased electron–hole pair separation, and as a consequence a better photocatalytic performance is achieved.

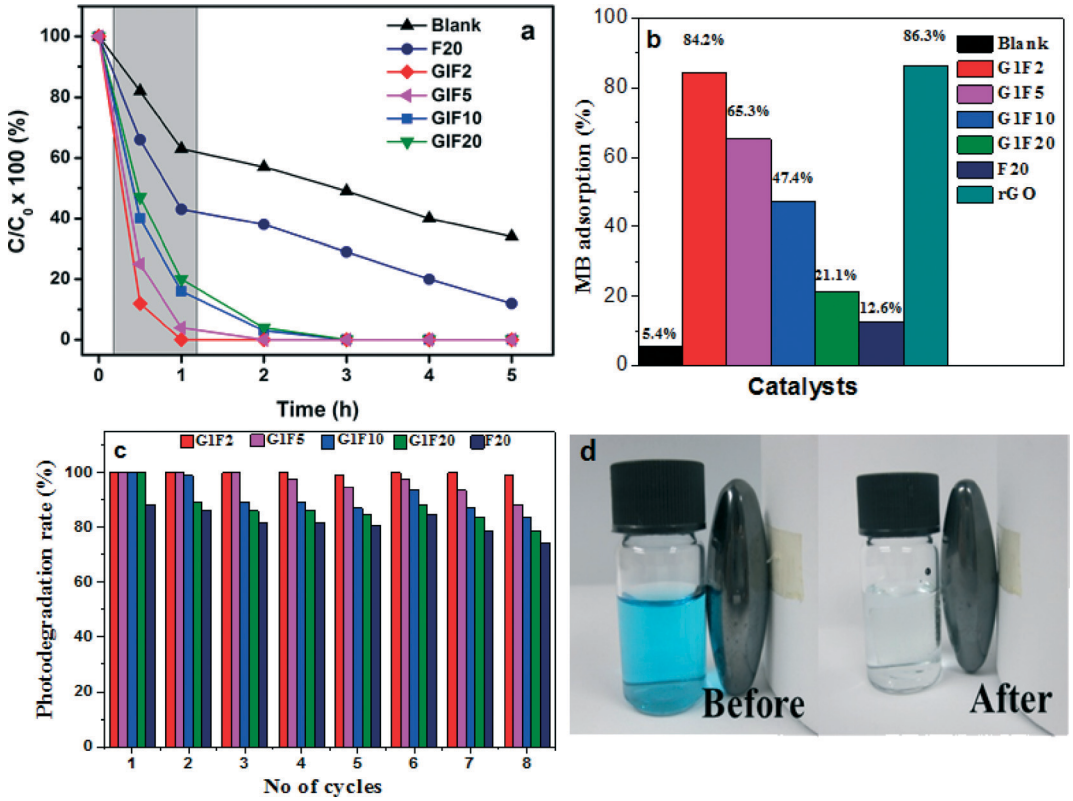

Fig. 7 Photocatalytic degradation of MB in the presence of different photocatalysts under sunlight irradiation (a). Adsorption of MB by different catalysts after 12 h stirring. (b). Photodegradation efficiency (%) of MB solution for 8 cycles in the presence of rGO/Fe_3O_4 nanocomposites and Fe_3O_4 (c). Photographic images of MB before and after degradation by rGO/Fe_3O_4 and recovery of the catalyst by applying an external magnet (d).

To further understand the enhanced photocatalytic performance of the rGO/Fe_3O_4 nanocomposites, the MB solution was continuously stirred with the photocatalysts overnight (12 h); the results are shown in Fig. 7(b). The rGO and GIF2 showed maximum adsorptions of ~86 and ~84%, respectively. Further increasing the Fe_3O_4 content in the nanocomposite led to a decrease in the adsorption of MB. The shadowed area in Fig. 7(a) follows a similar trend to the adsorption behaviour of the photocatalysts. The enhanced MB dye adsorptivity of the rGO/Fe_3O_4 photocatalysts is due to the large phenyl ring structure of the graphene[34,35] in the nanocomposites. Moreover, graphene is a 2D crystalline structure and has a large surface area, superior electrical conductivity and unique transport properties, making it a great electron-transport material in the process of photocatalysis. When Fe_3O_4 nanoparticles are anchored on the surface of graphene sheets, the graphene provides more adsorption sites and photocatalytic reaction centres for the MB dye molecules through the π–π conjugation and electrostatic attraction between the MB dye and the aromatic region of the graphene sheets.[36,37] These highly exposed surface active reaction sites are beneficial for promoting the generation of hydroxyl radicals for MB adsorption, by redox reactions within the active sites (Fe^{2+}/Fe^{3+}). Additionally, the strong Fe–O–C interactions of rGO/Fe_3O_4, between the delocalized unpaired π electrons from the π-conjugated carbon network on graphene's basal plane, facilities electron transfer between the rGO sheets and iron centres.[38] Notably, the photocatalytic activity is highly dependent on the concentration of photogenerated charge carriers during the reaction.[39] Therefore, the strong attachment of Fe_3O_4 on the electron carries of the rGO sheets gives rise to a enhanced migration of photoexcited electrons from the conduction band of Fe_3O_4 to the rGO sheets. The fast electron-transfer kinetics of rGO/Fe_3O_4 helps to improve the interfacial charge transfer process,[40] leading to enhanced photocatalytic activity. On the other hand, the strong anisotropic dipolar interactions of Fe_3O_4 in aqueous phase[41] are likely to diminish or restrict its catalytic activity, and thus the Fe_3O_4 nanoparticles are prone to aggregate into larger Fe_3O_4 particles (Fig. 1(b)), leading to decreased MB decolourization efficiency.

The sustainability of a photocatalyst is one of the most important requirements for successful practical applications. In this respect, the reusabilities of the rGO and rGO/Fe_3O_4 photocatalysts were investigated using the same photocatalyst for 8 sets of experiments, with fresh MB solution for each experiment, keeping all other experimental parameters constant. After each photodegradation experiment, the photocatalyst was removed from the photolysis cell using an external magnetic field and washed with high pure DI water, to remove the presence of any MB associated organic impurities. The magnetic separation technique represents an easy and convenient way to remove or recycle the photocatalyst.

This can be achieved by placing a magnet close to the sample bottle, which causes the rGO/Fe_3O_4 photocatalyst to move towards the external magnetic field and be attracted to the side of the bottle, leaving behind a clear reaction solution (Fig. 7(d)). Therefore, the rGO/Fe_3O_4 can be easily reused and recycled after the photocatalytic process. The MB dye molecules could be effectively photodecomposed in each experimental cycle and no significant change in the photocatalytic activity of the G1F2 nanocomposite was observed during the repeated photocatalytic experimental cycles (Fig. 7(c)).

Among the different photocatalysts, the G1F2 nanocomposite exhibited the best stability during photocatalytic degradation of MB dye; hence it can be applied as a recyclable photocatalyst. The lower the content of Fe_3O_4 nanoparticles in the nanocomposites, the smaller the particle sizes are, with a high surface area and without heavy aggregation of Fe_3O_4 nanoparticles. Therefore they can offer excellent decolourization activity. Hence, G1F2 contains the lowest amount of Fe_3O_4 nanoparticles, and so has smaller particle sizes with high specific surface area, offering a number of active sites for the adsorption and subsequent desorption of MB molecules in the nanocomposite. This favours the facile transport of photoexcited electrons to reach the surface reaction sites more easily[42] and thereby efficiently inhibits the recombination of photo-induced electron–hole pairs during the electron-transfer process. Thus, the higher photocatalytic activity and sustainability of this magnetically separable rGO/Fe_3O_4 nanocomposite is greatly beneficial for industrial waste water treatment processes.

The schematic representation of MB degradation in the presence of the magnetically separable rGO/Fe_3O_4 photocatalyst is shown in Fig. 8. Upon light irradiation, the Fe_3O_4 present on the rGO sheet surface undergoes charge separation that leads to promotion of valence band (VB) electrons into the conduction band (CB), leaving a hole in the VB (eqn (1)), whereas the MB molecules are excited to cationic MB radicals (MB*) (eqn (2)). These photogenerated electrons in the conduction band are instantaneously transferred to rGO sheets (eqn (3)), and are consequently captured by dissolved O_2 to generate reactive oxidation species such as $^{\bullet}OH$ and $O^{2\bullet-}$ (eqn (4)). On the other hand, the photoinduced holes are crucial for the oxidation process and adsorbents are effectively oxidized; usually the $Fe_3O_4(h^+)$ can react with adsorbed H_2O/OH^- to form strong hydroxyl radicals ($^{\bullet}OH$) (eqn (5)). Finally, these $^{\bullet}OH$ radicals oxidize the MB molecules adsorbed to CO_2 and H_2O (eqn (6))[43] *via* the π–π stacking/electrostatic interactions on the active sites of the rGO/Fe_3O_4 nanocomposites.

$$Fe_3O_4 + h\nu \rightarrow Fe_3O_4(e^- + h^+) \quad (1)$$

$$MB + h\nu \rightarrow MB^* \quad (2)$$

$$Fe_3O_4 + \text{graphene} \rightarrow Fe_3O_4 + \text{graphene}(e^-) \quad (3)$$

$$\text{Graphene}(e^-) + O_2 \rightarrow \text{graphene} + O^{2\bullet-} \quad (4)$$

$$Fe_3O_4(h^+) + OH^- \rightarrow Fe_3O_4 + {}^{\bullet}OH \quad (5)$$

$$MB^* + {}^{\bullet}OH \rightarrow CO_2 + H_2O \quad (6)$$

4. Conclusion

We have reported the preparation of photocatalysts based on magnetically separable rGO/Fe_3O_4 nanocomposite materials,

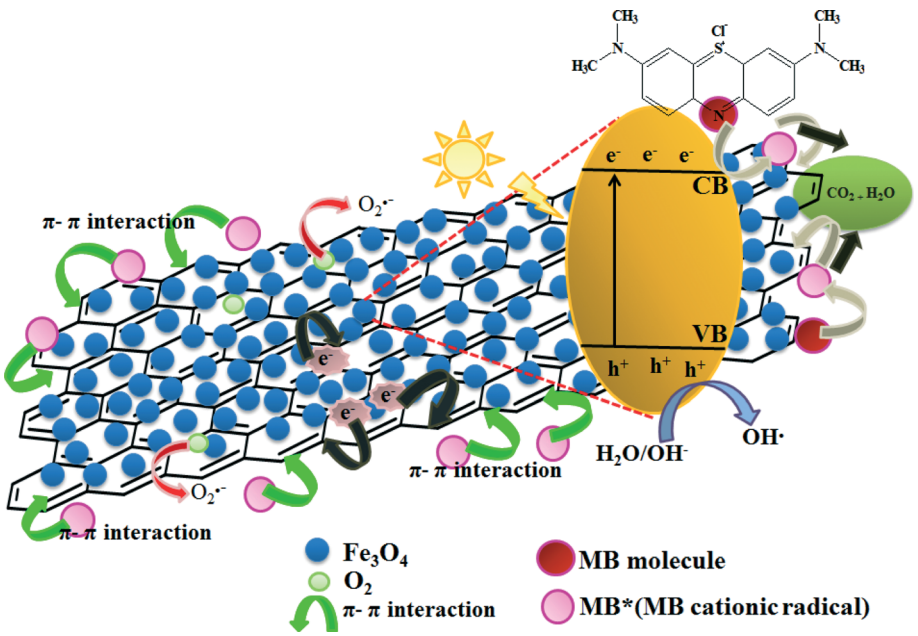

Fig. 8 Schematic representation of the photocatalytic degradation of MB in the rGO/Fe_3O_4 nanocomposites under natural sunlight irradiation.

through a simple, eco-friendly and cost-effective approach at room temperature. The obtained nanocomposite materials were characterized by various suitable techniques such as HRTEM, XRD, and VSM analyses, Raman spectroscopy, PL and UV-vis spectrophotometry. The XRD pattern indicated the formation of Fe_3O_4–rGO nanocomposites and the HRTEM images showed that the Fe_3O_4 nanoparticles with an average size of 10 nm were incorporated into the rGO sheets. The super-paramagnetic properties of the rGO/Fe_3O_4 nanocomposite materials were revealed through VSM analysis. This super-paramagnetic behaviour of the rGO/Fe_3O_4 nanocomposites is highly advantageous when designing a solid-solution system for photocatalytic applications, as it facilitates the simple physical separation of the catalyst from the solution, in contrast to the other colloidal photocatalyst systems. The rGO/Fe_3O_4 exhibited excellent adsorption behaviour and enhanced photocatalytic performances towards the degradation of methylene blue (MB) dye compared to other samples such as rGO and pristine Fe_3O_4 nanoparticles. This enhanced photocatalytic activity could be attributed to the emergence of synergistic effects between the rGO and Fe_3O_4 and also to the reduced charge recombination. The rGO/Fe_3O_4 possessed good sustainability even after eight cycles of MB photodegradation, and moreover the morphology of the photocatalyst was unaffected. These features of magnetically separable rGO/Fe_3O_4 make it a promising and recyclable photocatalyst for many environmental remediation applications.

Conflict of interests

The authors declares that there is no conflict of interests regarding the publication of this research article.

Acknowledgements

This work was financially supported by the Exploratory Research Grant Scheme (ER016-2011A), the Fundamental Research Grant Scheme (UKM-FST-07-FRGS0233-2010), and a High Impact Research Grant from the Ministry of Higher Education of Malaysia (UM.C/625/1/HIR/MOHE/05).

References

1 G. Williams, B. Seger and P. V. Kamat, *J. Am. Chem. Soc.*, 2008, **2**, 1487–1491.
2 X. M. Chen, G. H. Wu, Y. Q. Jiang, Y. R. Wang and X. Chen, *Analyst*, 2011, **136**, 4631–4640.
3 H. T. Hu, X. B. Wang, F. M. Liu, J. C. Wang and C. H. Xu, *Synth. Met.*, 2011, **161**, 404–410.
4 J. F. Shen, B. Yan, M. Shi, H. W. Ma, N. Li and M. X. Ye, *J. Mater. Chem.*, 2011, **21**, 3415–3421.
5 G. Z. Liao, S. Chen, X. Quan, H. T. Yu and H. M. Zhao, *J. Mater. Chem.*, 2012, **22**, 2721–2726.
6 M. S. A. Sher Shah, A. R. Park, K. Zhang, J. H. Park and P. J. Yoo, *ACS Appl. Mater. Interfaces*, 2012, **4**, 3893–3901.
7 J. Zhang, Z. Xiong and X. Zhao, *J. Mater. Chem.*, 2011, **21**, 3634–3640.
8 X. Y. Li, X. Wang, S. Y. Song, D. P. Liu and H. J. Zhang, *Chem. – Eur. J.*, 2012, **18**, 7601–7607.
9 Z. J. Luo, H. J. Tang, L. L. Qu, T. T. Han and X. Y. Wu, *CrystEngComm*, 2012, **14**, 5710–5713.
10 H. X. Wu, G. Gao, X. J. Zhou, Y. Zhang and S. W. Guo, *CrystEngComm*, 2012, **14**, 499–504.
11 D. M. Fouad and M. B. Mohamed, *J. Nanotechnol.*, 2011, 1–7, DOI: 10.1155/2011/416060.
12 C. M. Yu, L. L. Gou, X. H. Zhou, N. Bao and H. Y. Gu, *Electrochim. Acta*, 2011, **56**, 9056–9063.
13 E. M. Rodríguez, G. Fernández, P. M. Álvarez, R. Hernández and F. J. Beltrán, *Appl. Catal., B*, 2011, **102**, 572–583.
14 K. Wang, L. X. Yu, S. Yin, H. N. Li and H. M. Li, *Pure Appl. Chem.*, 2009, **81**, 2327–2335.
15 W. H. Shi, J. X. Zhu, D. H. Sim, Y. Y. Tay, Z. Y. Lu, X. J. Zhang, Y. Sharma, M. Srinivasan, H. Zhang, H. H. Hng and Q. Y. Yan, *J. Mater. Chem.*, 2011, **21**, 3422–3427.
16 Y. Fu and X. Wang, *Ind. Eng. Chem. Res.*, 2011, **50**, 7210–7218.
17 H. K. He and C. Gao, *ACS Appl. Mater. Interfaces*, 2011, **2**, 3201–3210.
18 J. J. Liang, Y. F. Xu, D. Sui, L. Zhang, Y. Huang, Y. F. Ma, F. F. Li and Y. S. Chen, *J. Phys. Chem. C*, 2010, **114**, 17465–17471.
19 Y. S. Fu, H. Q. Chen, X. Q. Sun and X. Wang, *Appl. Catal., B*, 2012, **111–112**, 280–287.
20 H. N. Lim, N. M. Huang, S. S. Lim, I. Harrison and C. H. Chia, *Int. J. Nanomed.*, 2011, **6**, 1817–1823.
21 X. W. Wang, H. W. Tan, Y. Yang, H. Wang, S. M. Wang, W. T. Zheng and Y. C. Liu, *J. Alloys Compd.*, 2012, **524**, 5–12.
22 M. Sathish, T. Tomai and I. Honma, *J. Power Sources*, 2012, **217**, 85–91.
23 V. Chandra, J. S. Park, Y. Chun, J. W. Lee, I. C. Hwang and K. S. Kim, *ACS Nano*, 2010, **4**, 3979–3986.
24 K. Ritter, M. S. Odziemkowski and R. W. Gillham, *J. Contam. Hydrol.*, 2002, **55**, 87–111.
25 L. L. Ren, S. Huang, W. Fan and T. X. Liu, *Appl. Surf. Sci.*, 2011, **258**, 1132–1138.
26 D. Beydoun, R. Amal, G. K.-C. Low and S. McEvoy, *J. Phys. Chem. B*, 2000, **104**, 4387–4396.
27 X. J. Liu, L. K. Pan, T. Lv, G. Zhu, T. Lu, Z. Sun and C. Q. Sun, *RSC Adv.*, 2011, **1**, 1245–1249.
28 Y. Zhang, G. Li, H. Lu, Q. Lv and Z. Sun, *RSC Adv.*, 2014, **4**, 7594–7600.
29 D. K. Padhi and K. Parida, *J. Mater. Chem. A*, 2014, **2**, 10300–10312.
30 L. Zhou, Y. Shao, J. Liu, Z. Ye, H. Zhang, J. Ma, Y. Jia, W. Gao and Y. Li, *ACS Appl. Mater. Interfaces*, 2014, **6**, 7275–7285.
31 Y. Fu and X. Wang, *Ind. Eng. Chem. Res.*, 2011, **50**, 7210–7218.
32 M. Gao, W. Li, J. Dong, Z. Zhang and B. Yang, *World J. Condens. Matter Phys.*, 2011, **1**, 49.
33 W. Wu, Q. G. He and C. Z. Jiang, *Nanoscale Res. Lett.*, 2008, **3**, 397–415.
34 Y. Matsumoto, M. Koinuma, S. Ida, S. Hayami, T. Taniguchi, K. Hatakeyama, H. Tateishi, Y. Watanabe and S. Amano, *J. Phys. Chem. C*, 2011, **115**, 19280–19286.

35 J. C. Qu, C. L. Ren, Y. L. Dong, Y. P. Chang, M. Zhou and X. G. Chen, *Chem. Eng. J.*, 2012, **211–212**, 412–420.
36 T. G. Xu, L. W. Zhang, H. Y. Cheng and Y. F. Zhu, *Appl. Catal., B*, 2011, **101**, 382–387.
37 Y. S. Fu, P. Xiong, H. Q. Chen, X. Q. Sun and X. Wang, *Ind. Eng. Chem. Res.*, 2012, **51**, 725–731.
38 K. Jasuja, J. Linn, S. Melton and V. Berry, *J. Phys. Chem. Lett.*, 2010, **1**, 1853–1860.
39 A. Mukherji, B. Seger, G. Q. Lu and L. Wang, *ACS Nano*, 2011, **5**, 3483–3492.
40 S. Saha, J. Wang and A. Pal, *Sep. Purif. Technol.*, 2012, **89**, 147–159.
41 J. Deng, X. Wen and Q. Wang, *Mater. Res. Bull.*, 2012, **47**, 3369–3376.
42 K. Parida, K. Reddy, S. Martha, D. Das and N. Biswal, *Int. J. Hydrogen Energy*, 2010, **35**, 12161–12168.
43 T. Harifi and M. Montazer, *Appl. Catal., A*, 2014, **473**, 104–115.